communications physics

Article

https://doi.org/10.1038/s42005-024-01644-3

Stoichiometric control of electron mobility and 2D superconductivity at $LaAlO_3$-$SrTiO_3$ interfaces

Check for updates

Gyanendra Singh [1] ✉, Roger Guzman [2], Guilhem Saïz[3], Wu Zhou [2], Jaume Gazquez[1], Fereshteh Masoudinia[1], Dag Winkler [4], Tord Claeson[4], Jordi Fraxedas [5], Nicolas Bergeal [3], Gervasi Herranz [1] & Alexei Kalaboukhov[4]

$SrTiO_3$-based conducting interfaces, which exhibit coexistence of gate-tunable 2D superconductivity and strong Rashba spin-orbit coupling (RSOC), are candidates to host topological superconductive phases. Yet, superconductivity is usually in the dirty limit, which tends to suppress nonconventional pairing and therefore challenges these expectations. Here we report on $LaAlO_3/SrTiO_3$ (LAO/STO) interfaces with large mobility and mean free paths comparable to the superconducting coherence length, approaching the clean limit for superconductivity. We further show that the carrier density, mobility, and formation of the superconducting condensate are controlled by the fine-tuning of La/Al chemical ratio in the LAO film. We find a region in the superconducting phase diagram where the critical temperature is not suppressed below the Lifshitz transition, at odds with previous experimental investigations. These findings point out the relevance of achieving a clean-limit regime to enhance the observation of unconventional pairing mechanisms in these systems.

The coexistence of two-dimensional (2D) superconductivity and spin-orbit-coupling (SOC) is key for the development of novel device concepts for quantum technologies that exploit unconventional electron pairing in topological phases[1,2]. Boundaries and defects in topological superconductors can host zero-energy Majorana modes, offering applications in quantum computation[3–8]. Although seminal proposals focused on hybrid superconductor-semiconductor structures[9,10], the simultaneous presence of superconductivity and large tunable SOC in $SrTiO_3$ quasi-two dimensional electron gases (q-2DEGs) offers a particularly appealing platform to explore unconventional and topological superconductive phases[11,12]. Particularly, q-2DEGs at the $LaAlO_3/SrTiO_3$ (LAO/STO) interface have been investigated intensively, where electrostatic gating allows to control the electron band filling within the t_{2g} manifold[13–15], enabling the electric field modulation of the superconducting phase diagram[16–22] and Rashba SOC[23–25]. Interestingly, the multiband character of the LAO/STO q-2DEG together with large Rashba SOC promotes the appearance of singlet-triplet mixed pairings, which, in the presence of magnetic fields, could lead to nontrivial superconductive states[26]. However, while Anderson's theorem holds for singlet pairing[27], disorder is expected to reduce triplet pairing, potentially hindering the emergence of topological phases. It is therefore indispensable to approach a clean limit for superconductivity at the LAO/STO q-2DEGs to enhance the chances of detecting nontrivial topological features in these systems[28].

In this work, we report on LAO/STO q-2DEGs with exceptionally large mobilities, which allow for achieving mean free paths (l_{mfp}) comparable to the superconductive coherence length (ξ), approaching the clean limit even in the depletion regime. In LAO/STO interfaces the electronic conductivity is ensured by t_{2g} electrons in Ti (d_{xy}, d_{xz}, d_{yz}) orbitals. The quantum confinement of the q-2DEG splits the energy levels of the 3d orbitals, whose splitting is dictated by the out-of-plane effective mass m^*, which depends on the degree of orbital wavefunctions overlapping along the confinement direction[29]. In conventional (001) oriented interfaces, the degenerated $d_{xz/yz}$ orbitals lie at higher energies, and their wave function delocalizes deeper into STO with a dielectric constant similar to that of the bulk. Electrons occupying these subbands encounter less scattering, resulting in higher electronic mobilities. In contrast, electrons in d_{xy} orbitals lie at lower energies and are confined near the interface where the dielectric constant is reduced by the interfacial electric field and shows smaller electronic mobility due to the

[1]Institut de Ciència de Materials de Barcelona (ICMAB-CSIC), Campus de la UAB, 08193 Bellaterra, Catalonia, Spain. [2]School of Physical Sciences, University of Chinese Academy of Sciences, Beijing 100049, China. [3]Laboratoire de Physique et d'Etude des Matériaux, ESPCI Paris, Université PSL, CNRS, Sorbonne Université, Paris, France. [4]Department of Microtechnology and Nanoscience - MC2, Chalmers University of Technology, SE 412 96 Gothenburg, Sweden. [5]Catalan Institute of Nanoscience and Nanotechnology (ICN2), CSIC and BIST, Campus UAB, Bellaterra, Barcelona 08193, Spain. ✉e-mail: gsingh@icmab.es

larger scattering caused by imperfections (Fig. 1b, c)[30–32]. The filling of these subbands can be precisely controlled with a gate voltage V_G by continuous and reversible doping of electrons at the quantum well and monitored by Hall effect[32]. The critical temperature T_c shows a dome-shaped phase diagram, first increasing at low doping in the depletion region and then going through a maximum T_c^{max} to subsequently reduce for further increasing V_G towards the overdoped region[16,17,21]. Attempts have been made to correlate this dome-shaped phase diagram with the filling of the subbands. It has been suggested that the superconducting order parameter emerges when electrons start filling $d_{xz/yz}$ subbands, whereas it is strongly suppressed or even absent below the Lifshitz transition[15,16,21,23,32–34]. In line with this argument, only one superconducting gap has been reported so far in (001)-oriented interfaces, implying the absence of d_{xy} superconductivity for this orientation[35]. This has precluded the investigation of the superconductivity of the (001) LAO/STO quantum well in the dilute regime, where one single band is occupied. We stress that in this region of phase diagram, the average electronic mobility for d_{xy} electrons usually reduces to $\mu_{d_{xy}} < 50$ cm^2/V.s, corresponding to a mean free path $l_{mfp} < 1$nm, which leads these systems to the extreme dirty limit[15,21,23,32–34]. As we discuss below, we reach mobilities around two orders of magnitude larger for d_{xy} electrons, which is crucial to observe superconductivity mediated by d_{xy} bands.

On the other hand, the origin of the 2DEG in LAO/STO interfaces has been discussed in terms of either oxygen vacancies[36–38] or polar discontinuity[39]. The former mechanism depends on external doping, while the latter mechanism is supported in view of the observation of conducting interfaces only beyond a critical thickness for LAO[40]. A dependence of the interfacial conductivity on cation stoichiometry of the LAO layer was observed by Warusawithana et al.[41], revealing that conductivity only appears in Al-rich LAO layers below a critical ratio La/Al < 0.97. However, how the variation of the La/Al ratio affects fundamental parameters such as carrier density, mobility or the superconducting transition remains an open issue. In this work, we have investigated the transport properties of LAO/STO interfaces that show a consistent variation of La/Al ratio and large mobilities μ ranging between 5×10^2–3×10^3 cm^2/Vs, at low electrostatic doping (i.e., in the depletion region of the quantum well) and between 5×10^3–2×10^4 cm^2/Vs at high doping (in the accumulation regime). These values are more than an order of magnitude larger than previously reported on superconducting interfaces[15,21,23,32–34]. We demonstrate that a small variation of the La/Al ratio in Al-rich $LaAlO_3$, as identified in X-ray photoelectron spectroscopy (XPS) and scanning transmission electron microscopy coupled with electron energy-loss spectroscopy (STEM-EELS) measurements, provides an excellent degree of freedom, in addition to electrostatic doping, to consistently alter carrier densities, mobilities and, remarkably, the onset of superconductivity. In contrast to previous reports, where superconductivity is either absent or suppressed below the Lifshitz transition[15,16,21,23,32–34], we observe a significant enhancement of T_c for

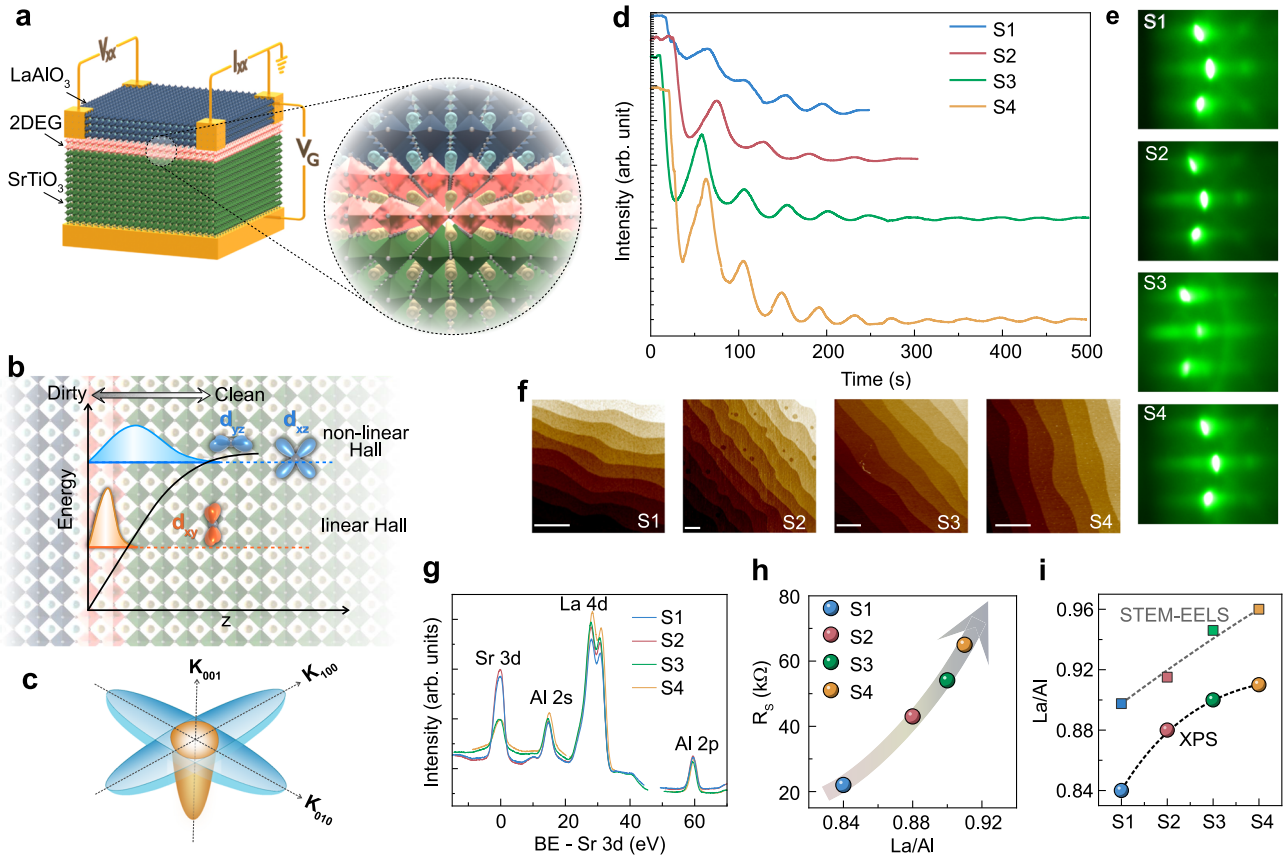

Fig. 1 | Schematic of the band structure and estimation of La/Al ratio using XPS. **a** Schematic illustration of $LaAlO_3/SrTiO_3$ (LAO/STO) heterostructure with two-dimensional electron gas (2DEG) at the interface. The zoomed-in view highlights the interfacial region of the crystal structure where the 2DEG exists. **b, c** Sketch of the quantum well in real and momentum space, respectively. Three non-degenerate t_{2g} orbitals split due to the confinement potential: the $d_{xz/yz}$ orbitals (blue) are shifted higher in energy compared to the d_{xy} orbitals (red). The conduction electrons, corresponding to d_{xy} orbitals, are closer to the interface, exhibiting lower electron mobility compared to the mobility for $d_{xz/yz}$ orbitals, which extend deeper into the STO. **d** The reflection high-energy electron diffraction (RHEED) intensity as a function of time, depicting a layer-by-layer growth, from which thickness can be inferred for the $LaAlO_3$ layer. **e** RHEED patterns obtained during the pulsed laser deposition (PLD) growth show a smooth film deposition. **f** Atomic force microscopy (AFM) topography images of a film. The well-aligned terraces indicate the surface smoothness. Scale bar: 500 nm. **g** The XPS spectra for all films. **h** The modulation of sheet resistance at room temperature as a function of the ratio of La/Al extracted from XPS spectra. **i** La/Al ratio in different samples extracted from scanning transmission electron microscopy coupled with electron energy-loss spectroscopy (STEM-EELS) and X-ray photoelectron spectroscopy (XPS) analysis.

electrostatic doping below the Lifshitz transition. We attribute this result to the large mobility, which allows the mean free path (at low doping) to be comparable to the superconducting coherence length (i.e. $l_{mfp} \sim \xi$), which is key to achieving d_{xy}-superconductivity.

Results

Film growth and characterization

Thin LAO films were grown by pulsed laser deposition (PLD) on top of (001) oriented TiO_2-terminated STO substrates (methods for growth process details). The epitaxial layer-by-layer growth of the films was confirmed by intensity oscillations of reflection high-energy electron diffraction (RHEED), as shown in Fig. 1d, e. Films were investigated by Atomic Force Microscopy (Fig. 1f), which showed a smooth surface with single-unit cell steps. The film composition of La/Al ratio was investigated using X-ray photoemission spectroscopy (XPS). Here, we present results for two 5-unit cell (uc) (S1 and S2), one 10 uc thick (S3) and one 11 uc (S4) thick film. Figure 1g shows XPS spectra of Sr 3d, La 4d, Al 2s, and Al 2p peaks for all samples. As expected, thicker films have much weaker intensity of substrate peaks (Ti and Sr). From the areas of La 4d and Al 2p peaks, we estimated the ratio between La and Al, assuming relative sensitivity factors of 6.52 and 0.54, correspondingly and with an error of about ~± 1% (methods for more details). Due to charging effects, the analysis required an alignment of the core levels to the position of the Sr 3d peak. The results show that all films are La deficient (Fig. 1i), in agreement with previously published results on films grown by PLD and MBE (Fig. 2k)[41]. The variation in the LAO film stoichiometry is likely due to the laser energy density during the film growth (Supplementary Fig. 1). More details about the influence of growth parameters on the film composition are discussed in supplementary note 1.

Figure 3 shows the high-angle annular dark field (HAADF) atomic resolution images (Fig. 3a, d, g, and j) of LAO/STO heterostructures along with the La M elemental maps (Fig. 3b, e, h, and k) and the resulting averaged La/Al ratios for each atomic plane (Fig. 3c, f, i, and l) obtained using

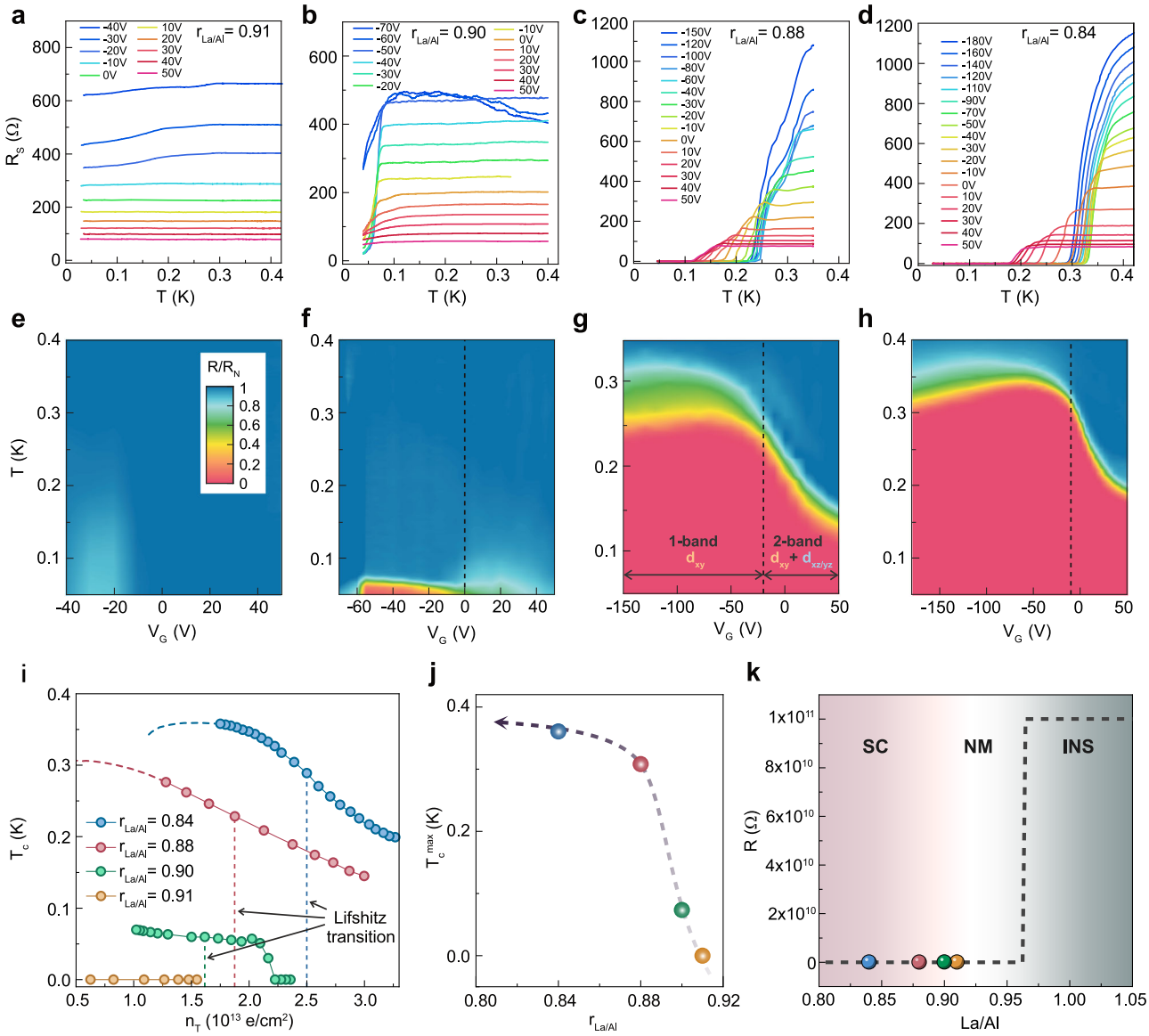

Fig. 2 | Superconducting phase diagram. a–d Resistance vs temperature curves measured between 0.4K - 0.03K at different gate voltage (V_G) for samples with $r_{La/Al}$ = 0.91, 0.90, 0.88, 0.84. **e–h** The corresponding color plot of normalized resistance as a function of temperature and V_G. The color scale is the same for all panels. The dashed line in color plot represents V_G for Lifshitz transition. **i** The modulation of critical temperature T_c as a function of total carrier density n_T. Here the carrier density corresponding to the dashed line is extracted from polynomial extrapolation of the data in Fig. 4i–l. **j** The variation of maximum of superconducting T_C^{max} with La/Al ratio. **k** The dashed line, adapted from ref. 41, indicates insulating-to-metallic transition as a function of La/Al ratio. The data points represented by circles correspond to the values of the La/Al ratio in our samples, as estimated from XPS analysis. The phase diagram is divided into three different regions: superconducting (SC), normal metal (NM), and insulating (INS) based on the outcome of our result.

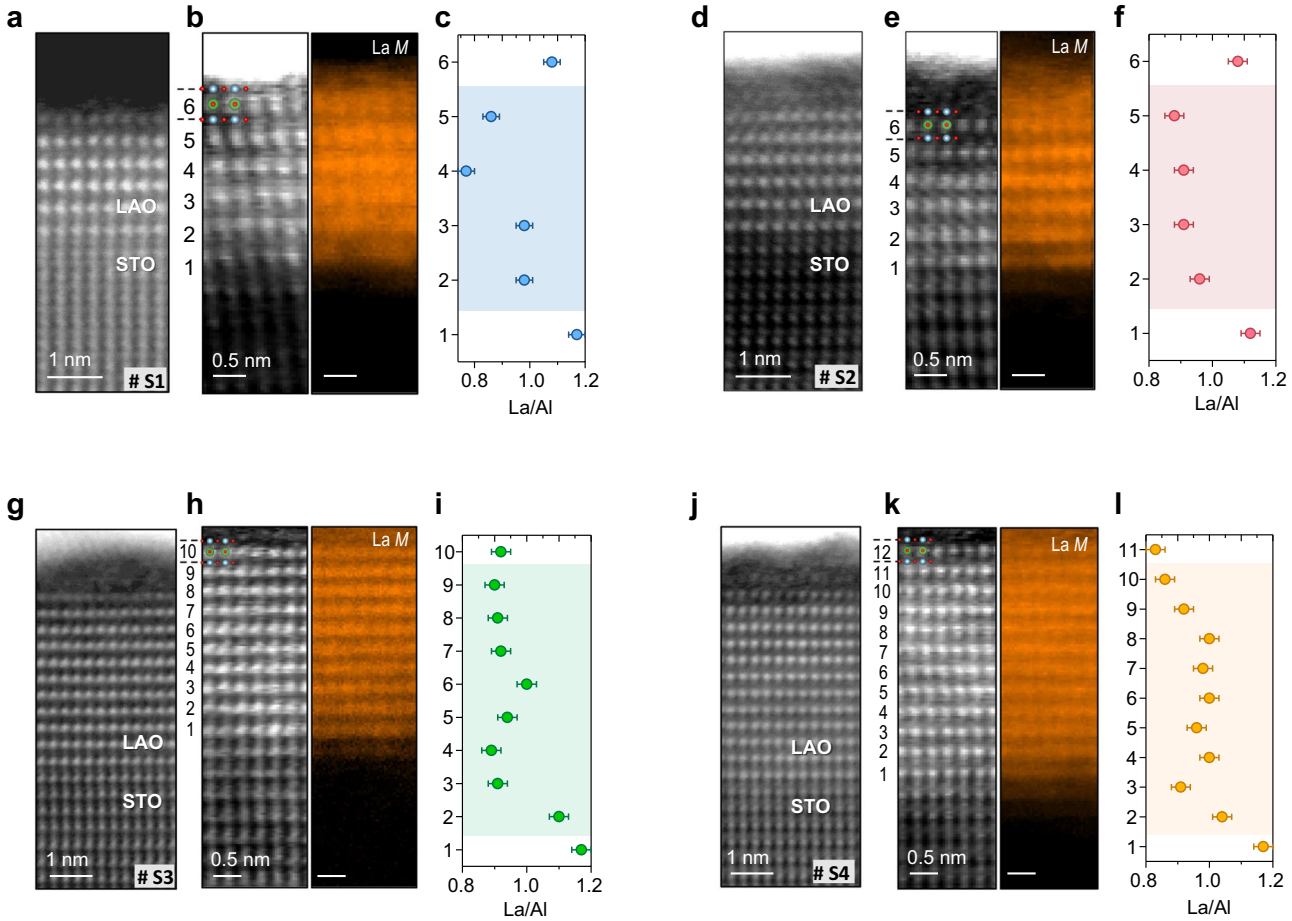

Fig. 3 | Estimation of La/Al ratio using STEM-EELS. The high-angle annular dark field (HAADF) atomic resolution image of LAO/STO interface, simultaneous ADF signal together with La elemental map and lateral averaged La/Al ratio of sample S1 (**a, b** and **c**), S2 (**d, e** and **f**), S3 (**g, h** and **i**) and S4 (**j, k** and **l**), respectively. The shaded region in **c, f, i, l** represents an area for which the average value of La/Al ratio is estimated. The error bars are estimated from the standard deviation with respect to the quantification fitting window parameters obtained from reference bulk LAO. The inset in **b, e, h,** and **k** shows the $LaAlO_3$ structure viewed along the [110] crystallographic direction, with La in green, Al in blue, and O in red.

EEL spectroscopy. These data indicate an inhomogeneous distribution of chemical composition, with a higher concentration of La near the interface in all samples, and at the uppermost plane of the 5 u.c thick LAO films of S1 and S2. The inhomogeneous distribution of La and Al near the interface can be caused by interdiffusion, which is evident from atomic-resolution elemental maps of all elements, including oxygen, see Supplementary Fig. 2. In particular, the Ti L-edge elemental maps show that Ti is substituting Al within the first LAO layer in all samples. The colored regions of the averaged La/Al ratio in Fig. 3c, f, i, and l show the atomic planes having a moderate deviation of the La/Al ratio. Figure 1i provides a depiction of the average La/Al ratio derived from the EEL spectrum images and compares it with XPS spectra. While the values obtained through EEL differ somewhat from those obtained via XPS, they exhibit a consistent overall trend. This disparity could be attributed to the fact that all the samples exhibit a heightened concentration of La at the interface, a phenomenon that XPS may not be sensitive enough to detect.

Electrical transport in normal state

The sheet resistance at T = 300 K decreases for smaller La/Al ratios (Fig. 1h), indicating a correlation between electrical transport and stoichiometry. Since it is well-established that the electrical resistivity of the properly annealed crystalline LAO/STO interface does not depend on the thickness of the LAO overlayer[42–44], thus the variation in electrical resistivity in our samples can be attributed to the difference in the La/Al ratio. We emphasize that all samples show a metallic behavior in all the analyzed range of temperatures (2K-300K), with little sign of an increase in resistance at low temperatures (see Supplementary Fig. 3), indicating the absence of weak localization effects[45]. As discussed below, this agrees with the remarkably large values of the electronic mobility observed in all samples. In addition, carrier density is almost temperature independent in the interval 2K-300 K (Supplementary Fig. 4) in contrast to the majority of reports where a large reduction of carrier density was observed at low temperatures attributed to charge freeze out on charged crystal defects such as oxygen vacancies[46]. This again proves the high quality of interfaces studied in this work.

We investigated the effect of the La/Al ratio ($r_{La/Al}$) on the evolution of carrier density at 2K as a function of back gate voltages V_G. In the depleted regime, corresponding to negative or low positive V_G, we found a linear response of the transverse Hall resistance R_H as a function of the applied out-of-plane magnetic field ($B_\perp$) in all samples (Fig. 4a–d). In contrast, in the overdoped regime, corresponding to large positive V_G, we observed non-linear $R_H(B_\perp)$, indicating that a second band is filled (Fig. 4e–h) as the V_G is increased. The transition from the linear to non-linear $R_H(B_\perp)$ is usually ascribed to a Lifshitz transition from d_{xy} single-band to $d_{xy} + d_{xz/yz}$ two-band transport regimes when the $d_{xz/yz}$ subband is occupied at higher V_G (see Fig. 1b, c for sketch of band structure). The transition can be better observed by obtaining the Hall carrier density $n_H = B_\perp/eR_H$ through linear fits of $R_H(B_\perp)$ in the limits $B_\perp < 0.5$T and $B_\perp > 4$T, respectively (Fig. 4i–l). The n_H overlap at low V_G in the linear regime (comparatively depleted region), in agreement with the single-band transport. In contrast, above the

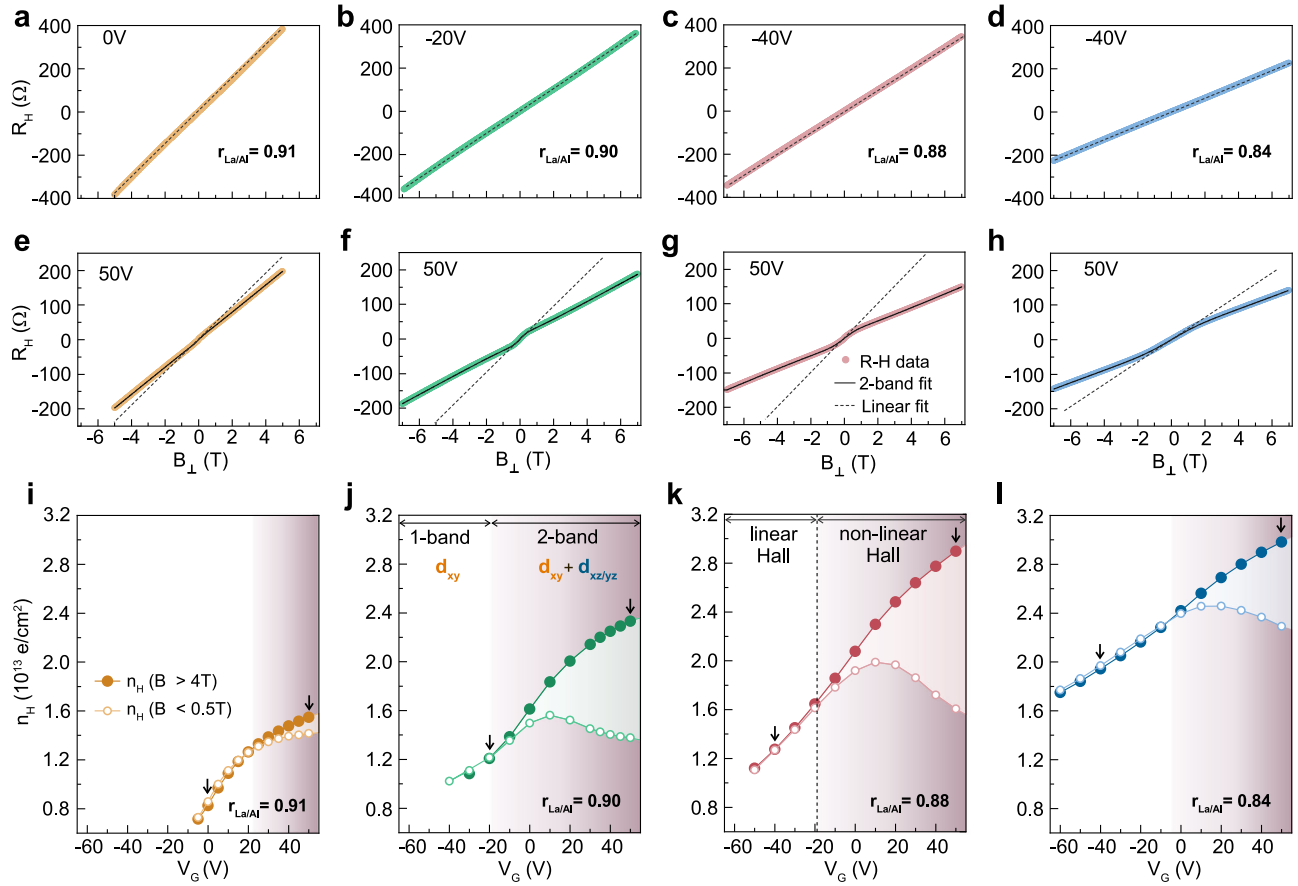

Fig. 4 | Gate voltage-dependent Hall carrier density. The Hall resistance as a function out-of-plane magnetic field, $R_H(B_\perp)$, for LAO/STO samples S4, S3, S2, and S1 with $r_{La/Al}$ = 0.91 (**a**, **e**), 0.90 (**b**, **f**), 0.88 (**c**, **g**), and 0.84 (**d**, **h**) respectively. This is within the low gate voltage (V_G) region of the phase diagram with linear dependence in $R_H(B_\perp)$ (**a**–**d**), and at 50V where $R_H(B_\perp)$ display nonlinear dependence (**e**–**h**). The black-dashed line indicates a linear fit of $R_H(B_\perp)$. The black solid line is a fit of the two-band model (eq 1 presented in methods). **i**-**l** The evolution of carrier density as a function of V_G extracted from the linear fit of $R_H(B_\perp)$ for $B_\perp < 0.5$T (open circle) and $B_\perp > 4$T (solid circle). The shaded area indicates the region of V_G where $R_H(B_\perp)$ is nonlinear i.e. two bands regime. In the shaded region, n($B_\perp < 0.5$T) vs. V_G curve is not representing the true value of carrier density due to nonlinear $R_H(B_\perp)$, whereas, n($B_\perp > 4$T) is nearly equal to total carrier density $n_T = n_{d_{xy}} + n_{d_{xz/yz}}$. Two arrows are the selection of gate voltage for which $R_H(B_\perp)$ curves are shown. All measurements were performed at T = 2K.

Lifshitz transition at larger V_G, the two values of the n_H deviate from each other.

In our samples, the nonlinearity is observed at rather low magnetic fields $B_\perp \leq 2$T, as can be seen in Fig. 4e–h. This is in contrast to previous reports that showed nonlinear behavior in $R_H(B_\perp)$ extending for magnetic fields $B_\perp > 5$T[21,23,32,33]. We can attribute this to the distinct values of the electronic mobility in our samples, which are one order of magnitude larger than in previous reports. This is supported by the quantitative analysis of carrier densities and mobilities for each 3d-subbands using two-band model fit (see methods for details).

Figure 5a displays the V_G dependence of the total carrier density n_T and the carrier densities $n_{d_{xy}}$ and $n_{d_{xz/yz}}$ for electrons occupying d_{xy} and $d_{xz/yz}$ subbands, respectively. Similarly, Fig. 5b shows the data for the electronic mobilities $\mu_{d_{xy}}$ and $\mu_{d_{xz/yz}}$ as a function of V_G. In agreement with previous reports, we find that the majority of carriers are populating the lower energy d_{xy} orbitals ($n_{d_{xy}} \gg n_{d_{xz/yz}}$)[21,23,32,33]. However, $n_{d_{xy}}(\mu_{d_{xy}})$ and $n_{d_{xz/yz}}(\mu_{d_{xz/yz}})$ display a systematic increase (decrease) with the reduction of the $r_{La/Al}$ ratio (Fig. 5a, b). The values of $\mu_{d_{xy}}$ and $\mu_{d_{xz/yz}}$ obtained in our samples are about 15 times larger than in previous reports[21,23,32,33]. This can be attributed to the cleaner interfaces obtained in the present case. In addition, the values of the carrier density in the $d_{xz/yz}$ band are significantly larger than those reported previously. For instance, in our samples with $r_{La/Al}$ = 0.88 and 0.84, the fraction of carriers in $d_{xz/yz}$ bands exceeds 20%, as compared to less than 2% observed in previous works[23,32,33]. This implies that a small variation of the $r_{La/Al}$ ratio strongly affects carrier densities and mobilities in both bands, providing an additional degree of freedom to electrostatic gating, where the range of doping is limited by dielectric properties of $SrTiO_3$.

Superconducting properties

To investigate superconductivity, we measured the temperature dependence of the sheet resistance $R_S(T)$ between 0.03 and 0.45 K for different V_G. Figure 2a–d show $R_S(T)$ curves at different V_G and Fig. 2e–h display the corresponding color plot of normalized resistance as a function of T and V_G. It is evident that the $r_{La/Al}$ has also a strong effect on the formation of superconducting ground state. The maximum of superconducting critical temperature T_C^{max}, extracted from T_C-V_G phase diagram, increases with reducing $r_{La/Al}$, as shown in the Fig. 2j. For $r_{La/Al}$ = 0.91, the interface does not display any evidence of superconducting transition for any V_G (Fig. 2a, e) despite being metallic down to the lowest temperature of 30 mK. A weak superconducting transition is observed for $r_{La/Al}$ = 0.90 with a $T_C^{max} \approx 0.08$ K at $V_G \approx -60$ V (Fig. 2b, f). In this sample, R_S saturates to a residual resistance at low temperature, suggesting the presence of non-percolating superconducting regions in the sample, as shown in Supplementary Fig. 5 where superconducting regions embedded in a metallic matrix are sketched. On the other hand, a clear zero-resistance state with $T_C^{max} \approx 0.25$K at $V_G < -50$ V is achieved in the $r_{La/Al}$ = 0.88 sample (Fig. 2c, g), where $R_S(T)$ displays a broad superconducting transition suggesting a competition between superconducting and metallic regions (Supplementary Fig. 5). Interestingly,

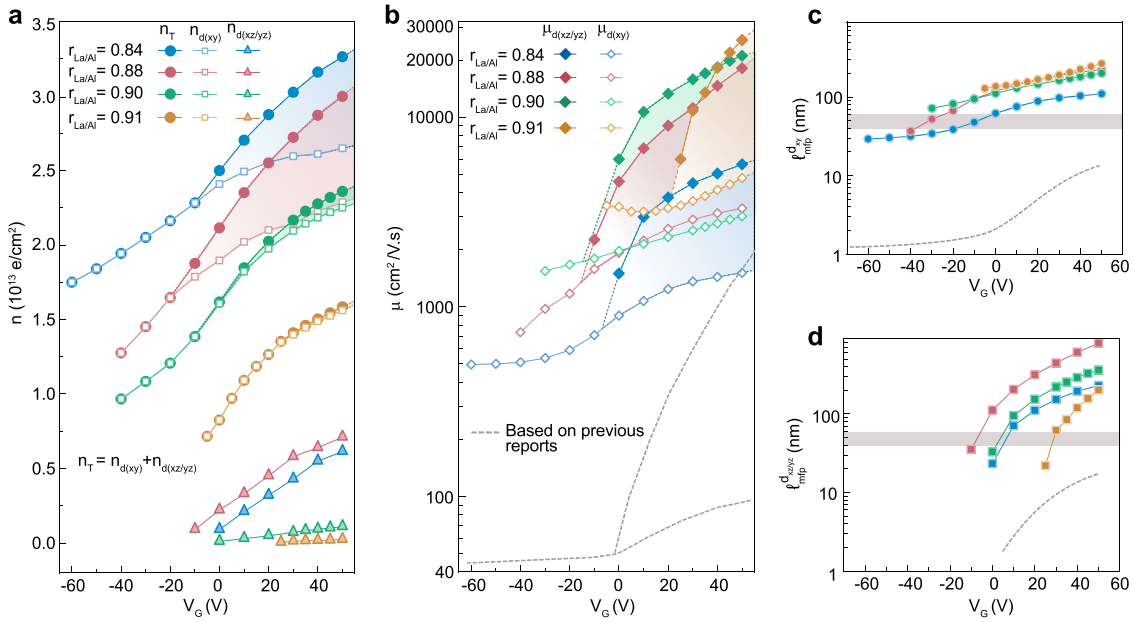

Fig. 5 | Estimation of carrier density and mobility in each t_{2g} band. a The evolution of total carrier density n_T (solid circle) and carrier density for electrons occupied in lower energy d_{xy} band, $n_{d(xy)}$, (open square) and upper $d_{xz/yz}$ band, $n_{d(xz/yz)}$ (solid triangle), as a function of V_G, extracted from two-band model fit. **b** The extracted values of corresponding electron mobility $\mu_{d(xy)}$ and $\mu_{d(xz/yz)}$ as a function of V_G. The shaded area represents two-band region in the phase diagram. **c**, **d** The estimated value of mean free path for d_{xy} electrons $l^{d_{xy}}_{mfp}$ and $d_{xz/yz}$ electrons $l^{d_{xz/yz}}_{mfp}$ respectively. The shaded gray area is the estimated value of coherence length adapted from ref. 15.

confirming a systematic trend, a sharp superconducting transition is observed in the samples with the lowest $r_{La/Al} = 0.84$, with $T_C^{max} \approx \approx 0.35$K at gate voltages $V_G \approx -50$ V (Fig. 2d, h).

Discussion

Our results provide important insights into the nature of superconductivity in the oxide q-2DEGs. According to the conventional Bardeen-Cooper-Schrieffer (BCS) scenario, pairing through $d_{xz/yz}$ rather than d_{xy} bands is more favorable for superconductivity due to the larger density of states of the former[47]. In line with this, both experimental and theoretical studies show either the absence or strong suppression of superconductivity in single d_{xy}-band 2DEGs, in a region of the phase diagram where the electronic mobility lies below $\mu_{d_{xy}} < 50$ cm^2/V.s[15,21,23,32–34]. In striking contrast, the critical temperature T_c of the samples analyzed in this work is not suppressed below the Lifshitz transition. As shown in the phase diagram in Fig. 2g and h, for samples with $r_{La/Al} = 0.88$ and 0.84, the T_c increases substantially already below the Lifshitz transition, rising to >15% at maximum T_c, and further suppressed for higher doping. We attribute this remarkable observation to the large mobility of electrons in the d_{xy} band, with values $\mu_{d_{xy}} > 600$ cm^2/V (Fig. 5b), i.e., more than an order of magnitude larger than usually reported elsewhere. Strikingly, as inferred from data displayed in Fig. 2i, the Lifshitz transition does not appear at a universal carrier density as suggested in previous observations[21], indicating that the formation of the quantum well may evolve differently for different samples. These observations demonstrate that superconductivity at the $LaAlO_3/SrTiO_3$ interface can be achieved in the clean limit, opposite to previous reports where it was only reported in the dirty limit[22,33], characterized by a reduced mean free path to $l_{mfp} < 1$ nm in the depleted region. Our data (Fig. 5c, d) show that the l_{mfp} in our samples is comparable to the ξ = 40-60 nm. This observation is important for the search of theoretically predicted topological superconductivity in these systems, as it should minimize drastically the detrimental effect of disorder on non-conventional electron pairing[12,20,26]. We also note that our results may allow studying pairing mechanism in single d_{xy}-band superconductivity in (001)-oriented $LaAlO_3/SrTiO_3$ interfaces in the dilute limit mediated by ferroelectric fluctuations through soft transverse optical phonons[48–54]. This is in line with recent observations of enhanced transition temperatures near the ferroelectric quantum critical point of $SrTiO_3$[55–59], and the possible co-existence of ferroelectricity and superconductivity[59,60]. Similar mechanisms have been proposed for the recently found superconductive $KTaO_3$ interfaces, in which pairing occurs in 5d instead of 3d orbitals[61]. In particular, a soft optical mode induced by the inversion-breaking at the interface has been suggested for inter-orbital paring, a mechanism that could be general for quantum paraelectric interfaces[62]. Finally, we also show that both electrical transport and superconductivity in the $LaAlO_3/SrTiO_3$ q-2DEG are systematically correlated with cation stoichiometry of the LAO film. While the exact mechanism of this effect cannot be elucidated from the existing data, it may be related to the intrinsic charge compensation by defects[41]. Remarkably, our sample with the highest La/Al ratio ($r_{La/Al}$ = 0.91, S4) has striking similarity with previously reported $SrCuO_2$-capped q-2DEG showing temperature-independent carrier concentration and very high electron mobilities of up to 4×10^4 cm^2/Vs, but no superconducting transition[46]. This suggests that the electrical transport in the LAO/STO interface is determined both by oxygen exchange kinetics and cation stoichiometry of the LAO film.

Methods

Thin films growth

Thin LAO films were grown on 5×5 mm^2 large TiO_2-terminated STO substrates by pulsed laser deposition (PLD). The laser spot area on the target was set to 2 mm^2. The laser fluence was varied by changing the energy, which was measured after the focusing lens. The laser beam optics was adjusted to provide a true image of the laser aperture on the target. All films were deposited at an oxygen pressure of 10^{-4} mbar and a heater temperature of 800 °C. The target-to-substrate distance was set to 50 mm. The laser repetition rate was 1 Hz, corresponding to the growth rate of 40–50 pulses per unit cell layer. After deposition, all samples were annealed to 600 °C at the oxygen pressure of 300 mbar for one hour to eliminate oxygen vacancies that could be produced in the STO substrate during the deposition process.

X-ray photoemission spectroscopy (XPS)

XPS measurements have been performed by using Al K_α X-ray source (E = 1486.6 eV) and Argus CU hemispherical electron spectrometer from Scienta Omicron AB, P.O. Box 15120, SE-750 15 Uppsala Sweden. Due to unavoidable charging effects, core level peaks in spectra for all samples have been aligned to the position of Sr 3d peak, see Fig. 1g. La/Al ratios of all samples were estimated from analysis of La 4d and Al 2p peak areas using Scofield database for relative sensitivity factors (RSF) for La and Al of 6.52 and 0.537, correspondingly [J. H. Scofield, Lawrence Livermore Lab. Rept 1973, UCRL-51326]. Each value of La/Al ratio is an average of 3 consecutive measurements. The corresponding error was estimated to be ± 1%.

Scanning transmission electron microscopy - electron energy-loss spectroscopy (STEM-EELS)

STEM-EELS was performed along the [110] pseudocubic zone axis in an aberration-corrected Nion U-Hermes 100, operated at 60 kV, and equipped with Dectris ELA direct electron detector, which offers improved detective quantum efficiencies, narrower point spread functions, and superior signal-to-noise ratios. The convergence semi-angle was 32 mrad, the probe current 20 pA, and the collection semi-angle 75 mrad. The elemental maps were generated with Digital Micrograph's EELS quantification tool. We used a reference EEL spectrum acquired from a control sample, a commercial LAO substrate. The background in the spectra was removed using a power law fit, followed by integrating the La M4, 5 (830 eV) and Al K (1560 eV) edges intensity by using integration windows with energy range of 900–1000 eV and 1575–1690 eV, respectively, excluding the near-edge fine structure in both cases. The fitting parameters were adjusted to obtain a La/Al elemental quantification of the control sample. The La/Al ratio of LAO thin films was calculated using the same procedure, and to neglect the influence of thickness and plural scattering in the quantification of all spectra in this work (including the reference) were acquired in regions with the same sample thickness (20 nm).

Hall carrier density and two-band model

The gate voltage-dependent Hall effect measurements were performed in Quantum Design PPMS system in Van der Pauw geometry. The Hall resistance ($R_H = V_H/I$ was measured as a function of out-of-plane magnetic field, swept between ± 7T. The carrier density $n_H = B/eR_H$, reported in Fig. 4 of the main text, is extracted from R_H in the magnetic field limit of B < 1T and B > 4T.

In the two-band regime analysis, reported in Fig. 5 of main text, the Hall resistance can be defined as

$$R_H = \frac{B}{e}\frac{\frac{n_{d_{xy}}\mu_{d_{xy}}^2}{1+\mu_{d_{xy}}^2 B^2}+\frac{n_{d_{xz/yz}}\mu_{d_{xz/yz}}^2}{1+\mu_{d_{xz/yz}}^2 B^2}}{\left[\frac{n_{d_{xy}}\mu_{d_{xy}}}{1+\mu_{d_{xy}}^2 B^2}+\frac{n_{d_{xz/yz}}\mu_{d_{xz/yz}}}{1+\mu_{d_{xz/yz}}^2 B^2}\right]+\left[\frac{n_{d_{xy}}\mu_{d_{xy}}^2 B}{1+\mu_{d_{xy}}^2 B^2}+\frac{n_{d_{xz/yz}}\mu_{d_{xz/yz}}^2 B}{1+\mu_{d_{xz/yz}}^2 B^2}\right]^2} \quad (1)$$

Where, $n_{d_{xy}}, n_{d_{xz/yz}}$ and $\mu_{d_{xy}}, \mu_{d_{xz/yz}}$ are carrier densities and mobilities related to d_{xy} and $d_{xz/yz}$ bands which are obtained by fitting $R_H(B_\perp)$ using constraints for total carrier density $n_T = n_{d_{xy}} + n_{d_{xz/yz}}$ and longitudinal resistance $\frac{1}{R_S} = e(n_{d_{xy}}\mu_{d_{xy}} + n_{d_{xz/yz}}\mu_{d_{xz/yz}})$.

Data availability

The data that support the findings of this study are available from the corresponding author upon reasonable request.

Code availability

The code that supports the findings of this study is available from the corresponding author upon reasonable request.

Received: 28 November 2023; Accepted: 23 April 2024;
Published online: 09 May 2024

References

1. Prada, E. et al. From Andreev to Majorana bound states in hybrid superconductor-semiconductor nanowires. *Nat. Rev. Phys.* **2**, 575 (2020).
2. Alicea, J. New directions in the pursuit of Majorana fermions in solid state systems. *Rep. Prog. Phys.* **75**, 076501 (2012).
3. Manchon, A., Koo, H. C., Nitta, J., Frolov, S. M. & Duine, R. A. New perspectives for Rashba spin-orbit coupling. *Nat. Mater.* **14**, 871 (2015).
4. Giustino, F. The 2021 quantum materials roadmap. *J. Phys. Mater.* **3**, 042006 (2020).
5. Mohanta, N. & Taraphder, A. Topological superconductivity and Majorana bound states at the $LaAlO_3/SrTiO_3$ interface. *Europhysics Letters* **108**, 6 (2014).
6. Mazziotti, M. V., Scopigno, N., Grilli, M. & Caprara, S. Majorana Fermions in One-Dimensional Structures at $LaAlO_3/SrTiO_3$ Oxide Interfaces. *Condens. Matter* **3**, 37 (2018).
7. Sato, M. & Yoichi, A. Topological superconductors: a review. *Rep. Progress Phys.* **80**, 076501 (2017).
8. Bernevig, B. A. *Topological insulators and topological superconductors*. (Princeton University Press 2013.)
9. Mourik, V. et al. Signatures of Majorana Fermions in Hybrid Superconductor-Semiconductor Nanowire Devices. *Science* **336**, 1003 (2012).
10. Lutchyn, R. M. et al. Majorana zero modes in superconductor-semiconductor heterostructures. *Nat. Rev. Mater.* **3**, 52 (2018).
11. Barthelemy, A. et al. Quasi-two-dimensional electron gas at the oxide interfaces for topological quantum physics. *Europhys. Lett.* **133**, 17001 (2021).
12. Perroni, C. A., Cataudella, V., Salluzzo, M., Cuoco, M. & Citro, R. Evolution of topological superconductivity by orbital-selective confinement in oxide nanowires. *Physical Review B* **100**, 094526 (2019).
13. Gariglio, S., Gabay, M. & Triscone, J. M. Research Update: Conductivity and beyond at the $LaAlO_3/SrTiO_3$ interface. *APL Mater.* **4**, 060701 (2016).
14. Salluzzo, M. et al. Orbital Reconstruction and the Two-Dimensional Electron Gas at the $LaAlO_3/SrTiO_3$ Interface. *Phys. Rev. Lett.* **102**, 166804 (2009).
15. Herranz, G. Engineering two-dimensional superconductivity and Rashba spin-orbit coupling in $LaAlO_3/SrTiO_3$ quantum wells by selective orbital occupancy. *Nat. Commun.* **6**, 6028 (2015).
16. Caviglia, A. D. et al. Electric field control of the $LaAlO_3/SrTiO_3$ interface ground state. *Nature* **456**, 624 (2008).
17. Hurand, S. et al. Field-effect control of superconductivity and Rashba spin-orbit coupling in top-gated $LaAlO_3/SrTiO_3$ devices. *Sci. Rep.* **5**, 12751 (2015).
18. Scheurer, M. S. & Schmalian, J. Topological superconductivity and unconventional pairing in oxide interfaces. *Nat. Commun.* **6**, 6005 (2015).
19. Stornaiuolo, D. et al. Signatures of unconventional superconductivity in the $LaAlO_3/SrTiO_3$ two-dimensional system. *Phys. Rev. B* **95**, 140502(R) (2017).
20. Singh, G. et al. Gate-tunable pairing channels in superconducting non-centrosymmetric oxides nanowires. *npj Quantum Mater.* **7**, 2 (2022).
21. Joshua, A., Pecker, S., Ruhman, J., Altman, E. & Ilani, S. A universal critical density underlying the physics of electrons at the $LaAlO_3/SrTiO_3$ interface. *Nat. Commun.* **3**, 1129 (2012).
22. Singh, G. et al. Gap suppression at a Lifshitz transition in a multi-condensate superconductor. *Nat. Mater.* **18**, 948 (2019).
23. Singh, G. et al. Effect of disorder on superconductivity and Rashba spin-orbit coupling in $LaAlO_3/SrTiO_3$ interfaces. *Phys. Rev. B* **96**, 024509 (2017).

24. Caviglia, A. D. et al. Tunable Rashba Spin-Orbit Interaction at Oxide Interfaces. *Phys. Rev. Lett.* **104**, 126803 (2010).
25. Shalom, M. B., Sachs, M., Rakhmilevitch, D., Palevski, A. & Dagan, Y. Tuning Spin-Orbit Coupling and Superconductivity at the $SrTiO_3$/$LaAlO_3$ Interface: A Magnetotransport Study. *Phys. Rev. Lett.* **104**, 126802 (2010).
26. Lepori, L., Giuliano, D., Nava, A. & Perroni, C. A. Interplay between singlet and triplet pairings in multiband two-dimensional oxide superconductors. *Physical Review B* **104**, 134509 (2021).
27. Anderson, P. W. Knight Shift in Superconductors. *Phys. Rev. Lett.* **3**, 325 (1959).
28. Jouan, A. et al. Quantized conductance in a one-dimensional ballistic oxide nanodevice. *Nat. Electron.* **3**, 201 (2020).
29. Santander-Syro, A. F. et al. Two-dimensional electron gas with universal subbands at the surface of $SrTiO_3$. *Nature* **469**, 189 (2011).
30. Berner, G. et al. Direct k-Space Mapping of the Electronic Structure in an Oxide-Oxide Interface. *Phys. Rev. Lett.* **110**, 247601 (2013).
31. Valentinis, D. et al. Modulation of the superconducting critical temperature due to quantum confinement at the $LaAlO_3$/$SrTiO_3$ interface. *Phys. Rev. B* **96**, 094518 (2017).
32. Biscaras, J. et al. Two-Dimensional Superconducting Phase in $LaTiO_3$/$SrTiO_3$ Heterostructures Induced by High-Mobility Carrier Doping. *Phys. Rev. Lett.* **108**, 247004 (2012).
33. Singh, G. et al. Competition between electron pairing and phase coherence in superconducting interfaces. *Nat. Commun.* **9**, 407 (2018).
34. Manca, N. et al. Bimodal Phase Diagram of the Superfluid Density in $LaAlO_3$/$SrTiO_3$ Revealed by an Interfacial Waveguide Resonator. *Phys. Rev. Lett.* **122**, 036801 (2019).
35. Richter, C. et al. Interface superconductor with gap behaviour like a high-temperature superconductor. *Nature* **502**, 528 (2013).
36. Herranz, G. et al. High Mobility in $LaAlO_3$/$SrTiO_3$ Heterostructures: Origin, Dimensionality, and Perspectives. *Phys. Rev. Lett.* **98**, 216803 (2007).
37. Kalabukhov, A. et al. Effect of oxygen vacancies in the $SrTiO_3$ substrate on the electrical properties of the $LaAlO_3$/$SrTiO_3$ interface. *Phys. Rev. B* **75**, 121404R (2007).
38. Siemons, W. et al. Origin of Charge Density at $LaAlO_3$ on $SrTiO_3$ Heterointerfaces: Possibility of Intrinsic Doping. *Phys. Rev. Lett.* **98**, 196802 (2007).
39. Nakagawa, N., Hwang, H. Y. & Muller, D. A. Why some interfaces cannot be sharp. *Nat. Mater.* **5**, 204 (2006).
40. Liping, Y. & Zunger, A. A polarity-induced defect mechanism for conductivity and magnetism at polar-nonpolar oxide interfaces. *Nature Communications* **5**, 5118 (2014).
41. Warusawithana, M. P. et al. $LaAlO_3$ stoichiometry is key to electron liquid formation at $LaAlO_3$/$SrTiO_3$ interfaces. *Nature Communications* **4**, 2351 (2013).
42. Thiel, S., Hammerl, G., Schmehl, A., Schneider, C. W. & Mannhart, J. Tunable Quasi-Two-Dimensional Electron Gases in Oxide Heterostructures. *Science* **313**, 1942 (2006).
43. Herranz, G., Sanchez, F., Dix, N., Scigaj, M. & Fontcuberta, J. High mobility conduction at (110) and (111) $LaAlO_3$/$SrTiO_3$ interfaces. *Sci. Rep.* **2**, 758 (2012).
44. Liu, Z. Q. et al. Origin of the Two-Dimensional Electron Gas at $LaAlO_3$/$SrTiO_3$ Interfaces: The Role of Oxygen Vacancies and Electronic Reconstruction. *Phys. Rev. X* **3**, 021010 (2013).
45. Biscaras, J. et al. Two-dimensional superconductivity at a Mott insulator/band insulator interface $LaTiO_3$/$SrTiO_3$. *Nat. Commun.* **1**, 89 (2010).
46. Huijben, M. et al. Defect Engineering in Oxide Heterostructures by Enhanced Oxygen Surface Exchange. *Adv. Funct. Mater.* **23**, 5240 (2013).
47. Bardeen, J., Cooper, L. N. & Schrieffer, J. R. Theory of Superconductivity. *Phys. Rev.* **108**, 1175 (1957).
48. Edge, J. M., Kedem, Y., Aschauer, U., Spaldin, N. A. & Balatsky, A. V. Quantum Critical Origin of the Superconducting Dome in $SrTiO_3$. *Phys. Rev. Lett.* **115**, 247002 (2015).
49. Kanasugi, S. & Yanase, Y. Spin-orbit-coupled ferroelectric superconductivity. *Phys. Rev. B* **98**, 024521 (2018).
50. Kanasugi, S. & Yanase, Y. Multiorbital ferroelectric superconductivity in doped $SrTiO_3$. *Phys. Rev. B* **100**, 094504 (2019).
51. Gastiasoro, M. N., Trevisan, T. V. & Fernandes, R. M. Anisotropic superconductivity mediated by ferroelectric fluctuations in cubic systems with spin-orbit coupling. *Phys. Rev. B* **101**, 174501 (2020).
52. Gastiasoro, M. N., Temperini, M. E., Barone, P. & Lorenzana, J. Theory of superconductivity mediated by Rashba coupling in incipient ferroelectrics. *Phys. Rev. B* **105**, 224503 (2022).
53. Yu, Y., Hwang, H. Y., Raghu, S. & Chung, S. B. Theory of superconductivity in doped quantum paraelectrics. *npj Quantum Mater.* **7**, 63 (2022).
54. Volkov, P. A., Chandra, P. & Coleman, P. Superconductivity from energy fluctuations in dilute quantum critical polar metals. *Nat. Commun.* **13**, 4599 (2022).
55. Stucky, A. et al. Isotope effect in superconducting n-doped $SrTiO_3$. *Sci. Rep.* **6**, 37582 (2016).
56. Tomioka, Y., Shirakawa, N., Shibuya, K. & Inoue, I. H. Enhanced superconductivity close to a non-magnetic quantum critical point in electron-doped strontium titanate. *Nat. Commun.* **10**, 738 (2019).
57. Ahadi, K. et al. Enhancing superconductivity in $SrTiO_3$ films with strain. *Sci. Adv.* **5**, eaaw0120 (2019).
58. Herrera, C. et al. Strain-engineered interaction of quantum polar and superconducting phases. *Phys. Rev. Materials* **3**, 124801 (2019).
59. Rischau, C. W. et al. A ferroelectric quantum phase transition inside the superconducting dome of $Sr_{1-x}Ca_xTiO_{3-\delta}$. *Nat. Phys.* **13**, 643 (2017).
60. Russell, R. et al. Ferroelectric enhancement of superconductivity in compressively strained $SrTiO_3$ films. *Phys. Rev. Materials* **3**, 091401 (2019).
61. Liu, C. et al. Two-dimensional superconductivity and anisotropic transport at $KTaO_3$ (111) interfaces. *Science* **371**, 716 (2021).
62. Liu, C. et al. Tunable superconductivity and its origin at $KTaO_3$ interfaces. *Nat. Commun.* **14**, 951 (2023).

Acknowledgements

The authors thank Kyle Shen and Jak Chakhalian for useful discussions. We acknowledge financial support from Projects No. PID2020-118479RB-I00, Severo Ochoa FUNFUTURE (No. CEX2019-000917-S) of the Spanish Ministry of Science and Innovation (Grant No.MCIN/AEI/10.13039/501100011033), project TED2021-129857B-I00 funded by MCIN/AEI/10.13039/501100011033 and by the European Union "NextGenerationEU"/PRTR and financial support by the Generalitat de Catalunya (2021 SGR00445). We also acknowledge support from the Swedish infrastructure for micro- and nanofabrication - MyFab. G.S. acknowledges financial support from the Beatriu de Pinós Programme with research Grant No. 2019 BP 00207 from the Secretariat for Universities and Research of the Department of Business and Knowledge of the Generalitat de Catalunya, and the support of the Marie Sklodowska-Curie program COFUND (BP3, contract no. 801370) of the H2020 programme. N.B. acknowledge the funding received by the ANR PRC (QUANTOP), by the QuantERA ERA-NET Cofund in Quantum Technologies (Grant Agreement N. 731473) implemented within the European Union's Horizon 2020 Program (QUANTOX), and by the French ANR PRC (SURIKAT ANR-23-CE30-0036).

The ICN2 is funded by the CERCA program/Generalitat de Catalunya. The ICN2 is supported by the Severo Ochoa Centres of Excellence programme, Grant CEX2021-001214-S, funded by MCIN/AEI/10.13039.501100011033. R.G. & W.Z. acknowledge financial support from National Key RD Program of China (2018YFA0305800), and the Beijing Outstanding Young Scientist Program (BJJWZYJH01201914430039).

Author contributions

G.Si. & A.K. conceived and directed the research. A.K. fabricated the samples and measured and analyzed XPS data. G.Si., G.S. and N.B. performed the transport measurements. G.Si. carried out the analysis of the transport results. R.G. and W.Z. performed and analyzed STEM-EELS data with the help of J.G. G.Si, G.H. and A.K. wrote the manuscript with the contribution of R.G., J.G., N.B., F.M., J.F., W.Z., T.C. and D.W. All authors have read and agreed to the published version of the manuscript.

Competing interests

The authors declare no competing interests.

Additional information

Supplementary information The online version contains supplementary material available at https://doi.org/10.1038/s42005-024-01644-3.

Correspondence and requests for materials should be addressed to Gyanendra Singh.

Peer review information *Communications Physics* thanks the anonymous reviewers for their contribution to the peer review of this work. A peer review file is available.

Reprints and permissions information is available at http://www.nature.com/reprints

Publisher's note Springer Nature remains neutral with regard to jurisdictional claims in published maps and institutional affiliations.

Open Access This article is licensed under a Creative Commons Attribution 4.0 International License, which permits use, sharing, adaptation, distribution and reproduction in any medium or format, as long as you give appropriate credit to the original author(s) and the source, provide a link to the Creative Commons licence, and indicate if changes were made. The images or other third party material in this article are included in the article's Creative Commons licence, unless indicated otherwise in a credit line to the material. If material is not included in the article's Creative Commons licence and your intended use is not permitted by statutory regulation or exceeds the permitted use, you will need to obtain permission directly from the copyright holder. To view a copy of this licence, visit http://creativecommons.org/licenses/by/4.0/.

© The Author(s) 2024